University of Bath

Alternative formats
If you require this document in an alternative format, please contact:
openaccess@bath.ac.uk

Nanococktail based on supramolecular glyco-assembly for eradicating tumors *in vivo*

Weiwei Feng,[a] Shangqian Zhang,[a] Yichen Wan,[a] Zelong Chen,[a] Yun Qu,[a] Jiahui Li,[a] Tony D. James,[b] Zhichao Pei,[a] and Yuxin Pei*,[a]

[a] Shaanxi Key Laboratory of Natural Products & Chemical Biology, College of Chemistry & Pharmacy, Northwest A&F University, Yangling, Shaanxi 712100, P. R. China

[b] Department of Chemistry, University of Bath, Bath, BA7 7AY, UK

ABSTRACT

The development of robust phototherapeutic strategies for eradicating tumors remains a significant challenge in the transfer of cancer phototherapy to clinical practice. Herein, a phototherapeutic nanococktail atovaquone/17-dimethylaminoethylamino-17-demethoxygeldanamycin/glyco-BODIPY (ADB) was developed to enhance photodynamic therapy (PDT) and photothermal therapy (PTT) via alleviation of hypoxia and thermal resistance, that was constructed using supramolecular self-assembly of glyco-BODIPY (BODIPY-SS-LAC, BSL-1), hypoxia reliever atovaquone (ATO) and heat shock protein inhibitor 17-dimethylaminoethylamino-17-demethoxygeldanamycin (17-DMAG). Benefitting from a glyco-targeting and glutathione (GSH) responsive units BSL-1, ADB can be rapidly

1

taken up by hepatoma cells, furthermore the loaded ATO and 17-DMAG can be released in original form into the cytoplasm. Using *in vitro* and *in vivo* results, it was confirmed that ADB enhanced the synergetic PDT and PTT upon irradiation using 685 nm near-infrared light (NIR) under a hypoxic tumor microenvironment where ATO can reduce O_2 consumption and 17-DMAG can down-regulate HSP90. Moreover, ADB exhibited good biosafety, and tumor eradication *in vivo*. Hence, this as-developed phototherapeutic nanococktail overcomes the substantial obstacles encountered by phototherapy in tumor treatment, and offers a promising approach for the eradication of tumors.

INTRODUCTION

The clinical treatment of cancer still faces numerous problems associated with unsatisfactory treatment effectiveness and damage to healthy tissues.[1-12] Phototherapy is noninvasive, exhibits minimal side effects, and is high selective and has been established as an excellent candidate for cancer treatment.[13-33] However, treatment efficacy is often unsatisfactory when phototherapy is used, due to limits imposed by the hypoxic tumor microenvironment (TME), including less O_2 that can decrease photodynamic efficacy and the up-regulated heat shock proteins (HSPs) may cause thermal resistance.[34-38] To overcome these obstacles, nano drug combinations called "nanococktails" comprising of photosensitizers and multiple units for the relief of hypoxia and the down-regulation of HSPs have been fabricated and utilized for cancer therapy. However, their construction remains challenging due to the utility of multiple components, requiring multi-step manufacturing, and potential systemic toxicity.[39-44]

Phototherapeutic nanococktail strategies are usually fabricated using various nanocarriers for direct oxygen (O_2) delivery, in situ generation of O_2 via decomposition of endogenous hydrogen peroxide (H_2O_2) or conversion of exogenous peroxides, and weakening O_2 consumption to refuel O_2 in the TME in order to boost the photodynamic therapy (PDT) efficacy.[45-47] While, HSPs inhibitors (including small interfering RNA (siRNA) and chemical inhibitors) are

commonly encapsulated in various phototherapeutic nanococktail based systems to downgrade the expression of HSPs, and thus amplify the sensitivity towards photothermal therapy (PTT).[48, 49] However, practical applications of hypoxia alleviators and HSPs inhibitors using nanococktail strategies are usually hindered by critical issues including loading capacity, nonspecific distribution, uncontrolled release, and cumulative potential toxicity, which mostly are attributed to the vehicles forming the basis of the nano therapeutic systems of nanococktails.[43, 50-56] As such clean and robust phototherapeutic nanococktail strategies exhibiting a good balance between safety and efficacy for tumor targeting and TME-control of synergetic PDT and PTT that can relieve hypoxia and down-regulate HSPs are ungently required.

The construction of phototherapeutic systems tends to be complicated and may lead to residual polymer, organic or inorganic materials, which requires a large number of toxicological studies during the clinical translation, increasing the difficulty of clinical translation.[57, 58] Multifunctional carrier-free nano-photosensitizers (NPSs) formed by supramolecular self-assembly of amphiphilic photosensitizer represent an effective synergistic PDT and PTT clinical translation strategy exhibiting many advantages, through integrating targeted delivery, TME-control release and synergistic PDT and PTT with single light illumination under ideal conditions.[59] Our group have established a glycosylated BODIPY-based tumor-specific and TME-responsive NPS, including a hydrophobic BODIPY, a hydrophilic lactose, and their linkage (a GSH-responsive disulfide bond), that can self-assemble into NPS for synergistic cancer PDT and PTT.[60] Based on analogous strategy of carrier-free multifunctional NPSs, cocktails of photosensitizer with dual inhibitors can be constructed by the simple loading of inhibitors into NPS.

In this work, a phototherapeutic nanococktail based on the supramolecular glyco-assembly of amphiphilic BSL-1 was fabricated, which was synthesized based on previously reported

procedures, using the efficient docking of hydrophobic BODIPY and the hydrophilic lactose moiety. BSL-1 could self-assemble with atovaquone (ATO, O_2 consumption inhibitor) and 17-dimethylaminoethylamino-17-demethoxygeldanamycin (17-DMAG, HSP90 inhibitor) to form phototherapeutic nanococktail ATO/17-DMAG/BSL-1 (ADB), which overcomes the inherent difficulty of the TME for phototherapy, influencing the efficacy of PDT and the thermal resistance to PTT at tumor sites. Once ADB enters hepatoma cells via glyco-targeting ability, BODIPY, ATO, and 17-DMAG are released via the reduction of disulfide bonds by high concentrations of GSH in tumor cells. Moreover, a HepG2 xenograft-bearing nude mice model indicated that the released moieties exhibit hypoxia relief, reactive oxygen species (ROS) generation, HSP90 down-regulation, and tumor eradication *in vivo*. We anticipate that nanococktails like ADB developed during this research represent an efficient green and safe phototherapeutic strategy exhibiting significant potential in the eradication of tumors.
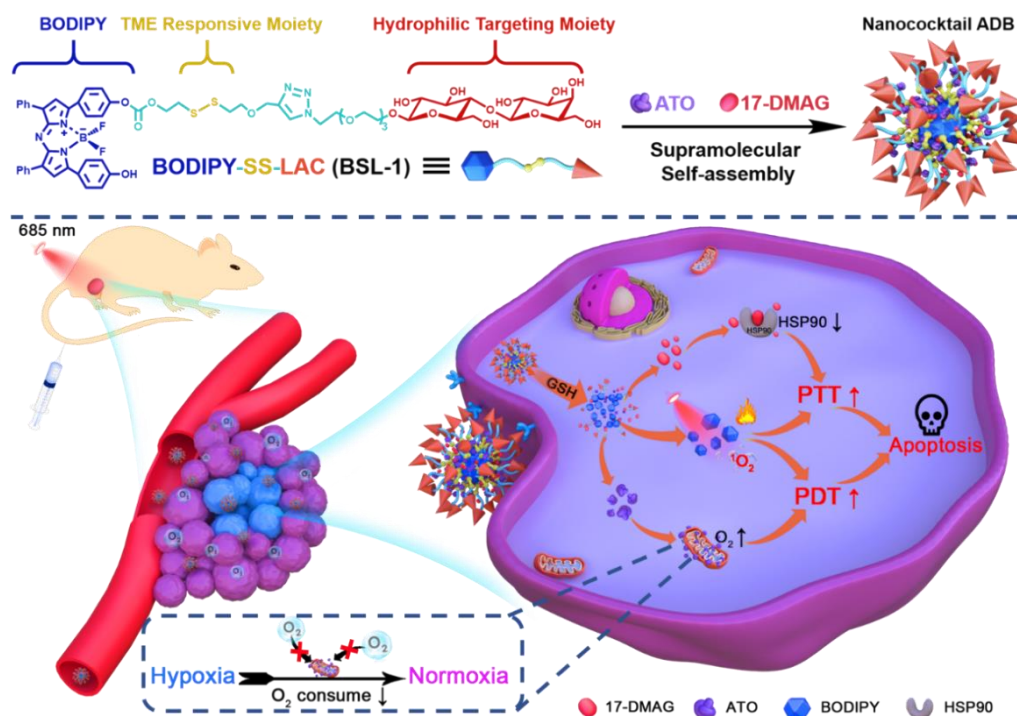
Scheme 1. Schematic illustration of nanococktail ADB constructed by supramolecular self-assembly of BSL-1, ATO and 17-DMAG for tumor selectivity and enhanced synergic PDT and PTT during hypoxia.

4

RESULTS AND DISCUSSION

Synthesis of BODIPY-SS-LAC (BSL-1). Compound **1** (BODIPY), SS (mono alkyne substituted 2,2'-dithiodiethanol) and LAC (a lactose azide derivative) were synthesized according to previous procedures.[60] As shown in Figure S1, compound **9**, a BODIPY derivative with one alkyne functional group linked by one disulfide bond, was synthesized in 44.2% yield by a one pot reaction of **1** and SS. Thereafter, BSL-1 was prepared by the CuAAC reaction of LAC and **9** in 76.5% yield. [1]H nuclear magnetic resonance (NMR), ^{13}C NMR, and high-resolution liquid chromatograph mass spectroscopy (HRLC-MS) were used for characterization of the synthesized compounds. In the supporting information, all the structural parameters are provided.

Construction and characterization of various nanococktails based on BSL-1. Critical aggregation concentration (CAC), transmission electron microscopy (TEM) and dynamic light scattering (DLS) were performed for evaluation of self-assembly of BSL-1 in water (water/DMSO, 1000:1, v/v). The CAC of BSL-1 in water was determined to be 9.83 μM (Figure S6). The size and morphology of the nano aggregates (B) formed from BSL-1 were evaluated using DLS (Figure 1a) and TEM (Figure 1b). Morphological characterization indicated that the amphiphilic BSL-1 can self-assemble into homogeneous nanoparticles in water. In Figure 1a, DLS analysis confirms that the average size of B is 115 nm, the polydispersity index is 0.281 and the average zeta potential is -24.2 mV.

BSL-1 can successfully self-assemble with ATO or/and 17-DMAG to construct various nanococktails, such as needle-shaped nano aggregate of ATO loaded BSL-1 (AB, Figure S7), leaf-shaped nano aggregate of 17-DMAG loaded BSL-1 (DB, Figure S8) and granular ADB (ADB, Figure 1d). The encapsulation efficiency of ATO and 17-DMAG in ADB are 91.65% and 11.95%, respectively; and the loading capacity are 19.45% and 4.52%, respectively. A double size distribution of 16.4 nm (20.5%) and 98.7 nm (79.5%) for ADB was analyzed,

resulting in average zeta potential of -16.8 mV via DLS (Figure 1c). Usually, nanoparticles with different particle sizes may affect their therapeutic effect via cell internalization.[61, 62] In our study, carbohydrate-mediated cellular uptake can enhance drug retention, which could reduce the effect of particle sizes on cellular uptake.[63] Therefore, the thus prepared ADB were used in the following experiments without further separation.

Meanwhile, the GSH responsiveness of BSL-1 was evaluated using ultraviolet-visible spectroscopy (UV/Vis), fluorescence spectroscopy, and DLS analysis. BSL-1 exposed to GSH exhibited a 32-nm red shift of the absorption peak in the UV/Vis spectrum and an increased emission peak of 730 nm in comparison with that of BSL-1, with overlapping of the absorption peak in UV/Vis spectra and emission peak in emission spectra with those of **1** in Figure S9 and Figure S10. GSH-treated nanococktail ADB exhibited aggregates with double size distribution of 305.8 nm (63.3%) and 5369 nm (36.7%) due to the GSH-reduced disulfide bond, which is quite different from that of ADB in Figure S11.
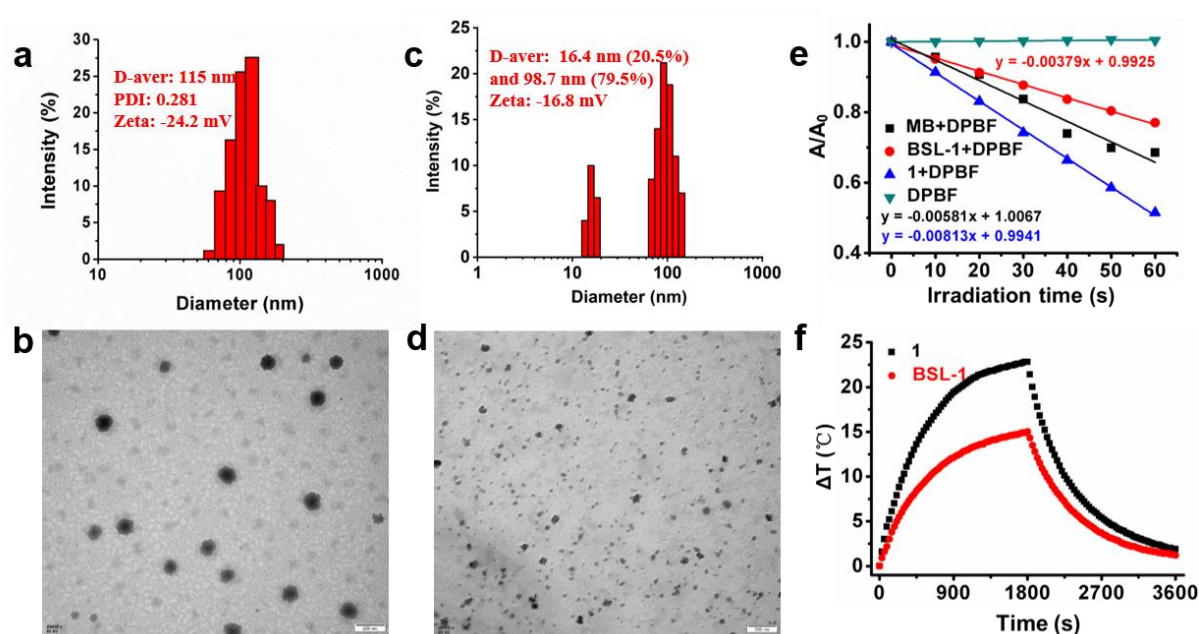
Figure 1. Characterization of nanococktails, photodynamic and photothermal properties. (a) DLS histogram of B (50 μM). (b) TEM photograph of B (50 μM). Scale bar, 200 nm. (c) DLS histogram of ADB (50 μM). (d) TEM photograph of ADB (50 μM). Scale bar, 200 nm. (e) ROS

6

generation of methylene blue (MB, 10 μM), BSL-1 (10 μM), and **1** (10 μM) measured with 1,3-diphenylisobenzofuran (DPBF, 30 μM) in water (0.08 W/cm^2, 60 s). (f) Photothermal conversion of **1** (10 μM) and BSL-1 (10 μM) in water (1.5 W/cm^2, 30 min).

ROS generation. The $^1O_2$ generation of BSL-1 and **1** under 685 nm NIR irradiation was measured with 1,3-diphenylisobenzofuran (DPBF). We used **1** instead of BSL-1 to determine the $^1O_2$ generation of BSL-1 treated with GSH, eliminating the effect of residual GSH on the amount of $^1O_2$.[60] As shown in Figure S12, except for DPBF itself, the absorption of DPBF at 422 nm in all experimental groups exhibited a decrease, which indicates the generation of $^1O_2$. MB as reference ($^1O_2$ quantum yields: $\Phi = 0.52$ in water), the $^1O_2$ quantum yields (Φ) of **1** and BSL-1 were calculated to be 0.317 and 0.183, respectively (Figure 1e).[64] The results indicated that after being released from B and degraded by GSH in cells, **1** can trigger enhanced production of $^1O_2$ compared with B, which is valuable for reducing the normal-tissues damage.

Photothermal conversion. The photothermal conversion efficiency of **1** and BSL-1 were measured to evaluate photothermal nature of **1** and BSL-1, in which NIR irradiation (1.5 W/cm^2, 30 min) was performed. The temperature of 8 mL **1** and BSL-1 in water increased by 22.8 °C and 14.7 °C, respectively (Figure 1f). This indicated that the light-to-heat conversion capacity of **1** is better than that of BSL-1. According to the previously reported calculation method,[65] from Figure S13, the photothermal conversion efficiency of **1** and BSL-1 were calculated to be 53.4% and 41.4%, which further confirmed that **1** released in the tumor microenvironment has stronger photothermal conversion ability than that of BSL-1. In addition, five laser on/off cycles of GSH-treated BSL-1 (Figure S14) suggested good photothermal stability of GSH-treated BSL-1.

Hepatocellular uptake of B. Since the hydrophilic module in the BSL-1 molecule is a lactose molecule, a lactose-enriched hydrophilic layer is naturally formed on the surface of self-

assembled B, which is effective for hepatoma cells targeting via overexpressed galectin in the cell membrane. The internalization of B was investigated by detecting the fluorescence of intracellular **1** using CLSM and FCM. With an increase in the co-incubation time, the fluorescence of **1** increased (Figure 2a, 2b, and 2d). From Figure 2b, B is clearly taken up by cells more easily than free **1**. The targeting ability of B was also determined using CLSM. In Figure 2c and 2e, the fluorescence in HepG2 cells was significantly stronger than that in HL7702 and HeLa. Meanwhile, the LBA pre-treatment significantly inhibited the cell uptake of B in HepG2 cells.
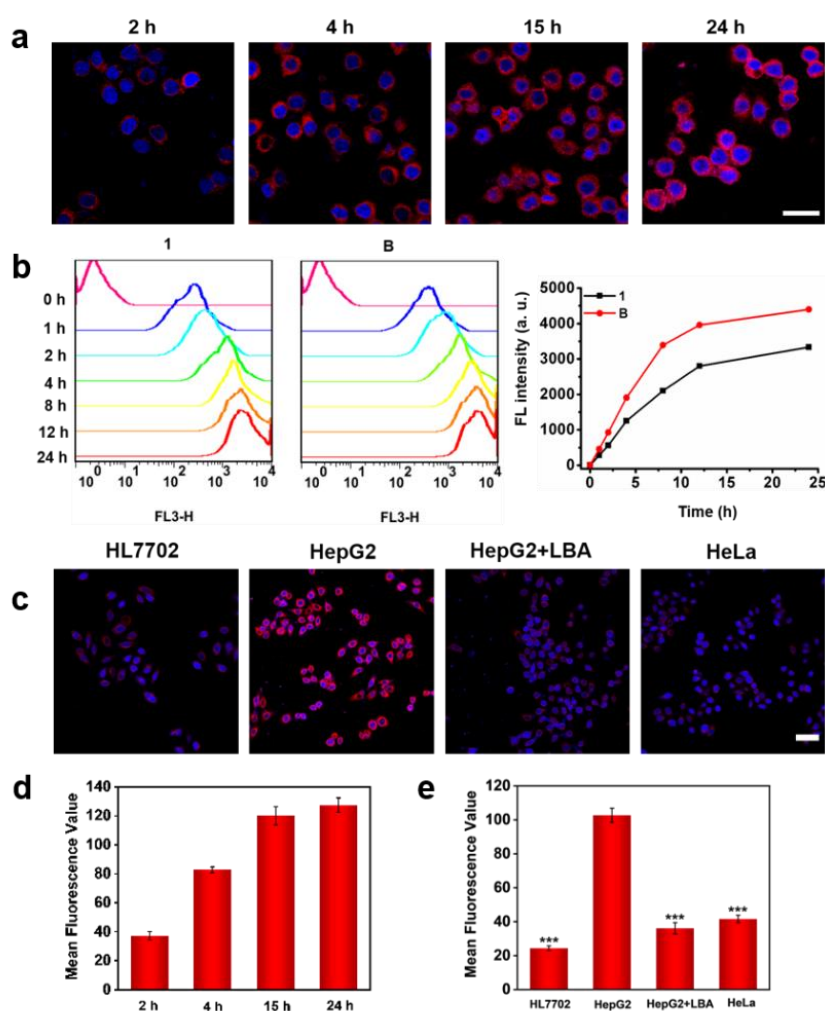
Figure 2. Cellular uptake in HepG2 and hepatoma cell targeting ability. (a) Cellular uptake detected by CLSM. (b) Cellular uptake of **1** and B detected by FCM. (c) Targeting ability of B was detected using CLSM. The treatment from left to right: HL7702, HepG2, HepG2 pre-

treated with lactobionic acid (HepG2+LBA), and HeLa. (d) Mean fluorescence intensity quantification of B in (a) (n = 3). (e) Mean fluorescence intensity quantification of B in (c) (n = 3), ***$P < 0.001$. The concentrations of **1** and BSL-1 were both 2.5 μM. Scale bar, 50 μm. For B, Ex/Em: 637/730 nm; for Hoechst, Ex/Em: 405/461 nm.
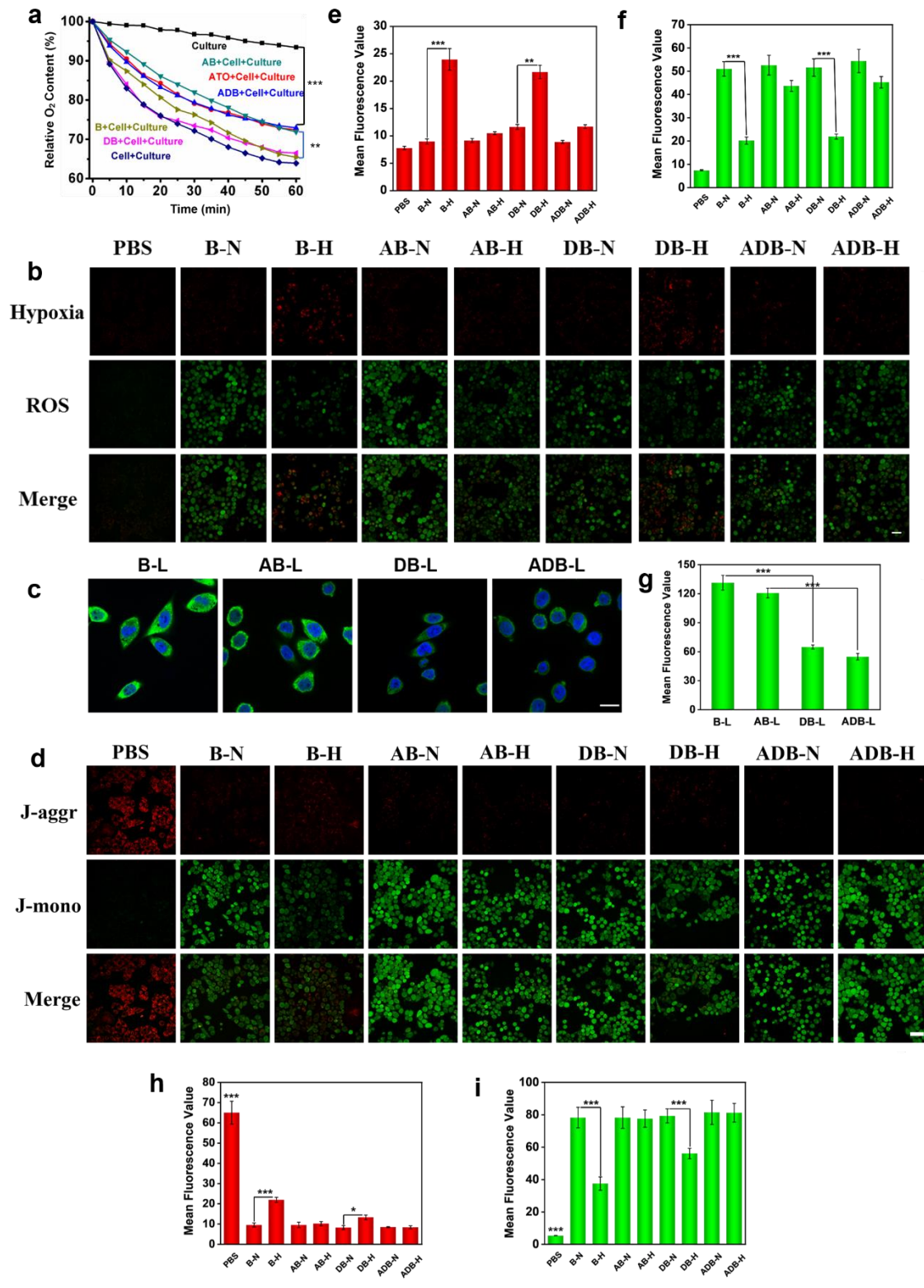
Figure 3. Hypoxia, ROS generation, HSP90 expression and mitochondrial membrane potential assays in HepG2 cells. (a) Changes in dissolved oxygen in cell cultures: Culture, ATO+Cell+Culture, ADB+Cell+Culture, AB+Cell+Culture, DB+Cell+Culture, B+Cell+Culture, and Cell+Culture; all groups need to be sealed with liquid paraffin (n = 3),

**P < 0.01, ***P < 0.001. (b) Hypoxia and ROS detection: PBS, B-N, B-H, AB-N, AB-H, DB-N, DB-H, ADB-N, and ADB-H (685 nm, 0.08 W/cm^2, 20 min; N: normoxia, H: hypoxia). Scale bar, 50 μm. (c) Expression of HSP90 in different groups: B-L, AB-L, DB-L, and ADB-L (685 nm, 0.08 W/cm^2, 20 min). Scale bar, 20 μm. (d) Mitochondrial membrane potential analysis: PBS, B-N, B-H, AB-N, AB-H, DB-N, DB-H, ADB-N, and ADB-H (685 nm, 0.08 W/cm^2, 20 min; N: normoxia, H: hypoxia). Scale bar, 50 μm. Mean fluorescence intensity quantification of hypoxia (e), and ROS (f) in (b) (n = 3), **P < 0.01, ***P < 0.001. (g) Mean fluorescence intensity quantification of HSP90 in (c) (n = 3), ***P < 0.001. Mean fluorescence intensity quantification of JC-aggr (h), and JC-mono (i) in (d) (n = 3), *P < 0.05, ***P < 0.001.

Hypoxia detection and ROS generation *in vitro*. Since hypoxia will limit the efficacy of PDT, it is essential for PDT efficacy that the nanococktail cause remission in hypoxia. The dissolved O$_2$ concentration of the cell culture medium of different groups can be measured using the dissolved O$_2$ detector. The changes of dissolved O$_2$ concentration in each group reflects the O$_2$ consumption by cell respiration, as shown in Figure 3a. In the ATO, ADB, and AB groups, the decline of the dissolved O$_2$ concentration is less than that for the groups without ATO. Therefore, ATO can indeed inhibit the O$_2$ consumption of cells. It indicates that the AB and ADB groups loaded with ATO can suppress O$_2$ consumption. Subsequently, a hypoxia and ROS detection kit was used to detect the levels of hypoxia and ROS in different groups. In Figure 3b and 3e, in all the normoxic groups, the hypoxia probe did not display strong red fluorescence. Meanwhile, in the hypoxic groups, we did not detect strong red fluorescence in AB and ADB groups with ATO. However, red fluorescence of the hypoxia probe in B and DB groups was stronger than that of all other groups, which indicates that the AB and ADB groups loaded with ATO exhibit a good effect on alleviating hypoxia. Similarly, the green fluorescence of the ROS detection probe displayed a strong green signal for the normoxic groups with NIR treatment, but in the hypoxic groups, enhanced green fluorescence is only detected for the AB and ADB groups in

Figure 3b and 3f, which indicates that the ATO in AB and ADB groups can reduce the O_2 consumption of cells, thereby alleviating hypoxia, and increasing the generation of ROS thereby enhancing the efficacy of PDT.

HSP90 expression assay *in vitro*. Heat shock protein (HSP) is a widespread heat stress protein. When the organism is exposed to high temperature, HSP is quickly expressed to protect the organism. HSP90 is an important member in the HSP family, and it is inextricably linked with the development of tumors. With this research, we analyzed the expression levels of HSP90 in cells treated with B-L, AB-L, DB-L and ADB-L under NIR irradiation by immunofluorescence. As shown in Figure 3c and 3g, in the B-L and AB-L groups, strong green fluorescence can be monitored in HepG2 cells, indicating that the HSP90 expression is up-regulated. While for the DB-L and ADB-L groups, the green fluorescence signal monitored in HepG2 cells was weak. Obviously, in the DB and ADB groups, the HSP90 inhibitor 17-DMAG was included, which influenced the expression of HSP90. Finally, the heat resistance of cancer cells can be overcome by the downregulation of HSP expression.

Depolarization of mitochondrial membrane potential. Mitochondrial permeable dye (JC-10) has unique distribution characteristics in cell mitochondria and can be used to measure the depolarization of the mitochondrial membrane potential. In normal cells, the mitochondrial membrane potential is high, and J aggregates of JC-10 are formed with red fluorescence in the mitochondrial matrix. When the mitochondrial membrane potential is low, JC-10 exists as a monomer with green fluorescence. As shown in Figure 3d, 3h and 3i, for each nanococktail when treated with NIR relatively strong green fluorescence could be detected. However, for the B-L hypoxia group, weak green fluorescence and red fluorescence was detected. In other groups, strong green fluorescence was observed without red fluorescence. Hypoxia limits the generation of ROS, thus the depolarization of mitochondrial membrane potential is affected, as such the membrane potential is higher than that of other groups.

Cell viability and apoptosis. To study the biocompatibility and anti-cancer activity of nanococktails, cell viability can be assessed using MTT analysis. We selected two cell lines for cell viability experiments: human normal hepatocytes HL7702 and hepatoma cells HepG2. As shown in Figure S15, even if the concentration of B is as high as 20 µM, the cell viability of HL7702 cells without NIR remains above 90%, while the cell viability of HepG2 remains at about 80%. B does not show strong cytotoxicity without NIR and exhibits good biocompatibility as a vehicle for drug delivery. At the same time, we compared the dark toxicity of ATO, 17-DMAG, and various nanococktails towards HepG2 and HL7702 cells. As shown in Figure S16, ATO is not toxic, and 17-DMAG shows strong toxicity to HepG2. However, after loading with B, their toxicity can be significantly reduced. As shown in Figure 4c, ATO and 17-DMAG are slightly toxic towards HL7702 at 4.58 and 0.6 µM, respectively. However, after loading with B, their cell toxicity was reduced, especially that for dual drug-delivery system ADB.
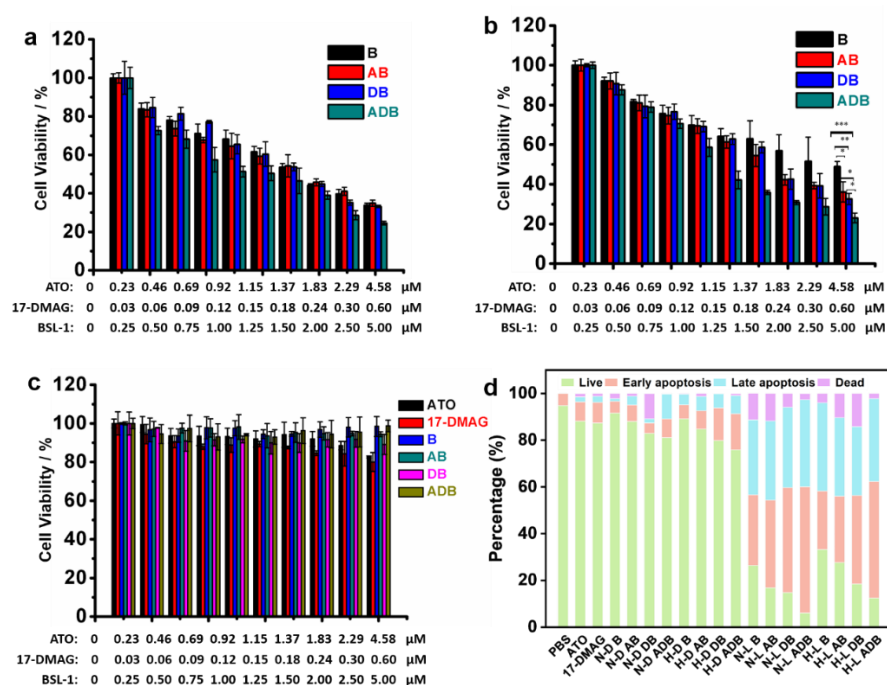

Figure 4. The cytotoxicity of various nanococktails. Cytotoxicity of B, AB, DB, and ADB to HepG2 cells under NIR: (a) normoxia and (b) hypoxia; NIR (685 nm, 0.08 W/cm^2, 20 min) (n

13

= 6), *P < 0.05, **P < 0.01, ***P < 0.001. (c) The biocompatibility of ATO, 17-DMAG, and various nanococktails to HL7702 cells (n =6). (d) Apoptosis assay of HepG2 cells: PBS, ATO, 17-DMAG, N-D B, N-D AB, N-D DB, N-D ADB, H-D B, H-D AB, H-D DB, H-D ADB, N-L B, N-L AB, N-L DB, N-L ADB, H-L B, H-L AB, H-L DB, and H-L ADB; N-D: normoxia without NIR, H-L: hypoxia with NIR, N-L: normoxia with NIR.

In the study of the phototoxicity of different nanococktails towards HepG2, the hypoxia was simulated by paraffin liquid sealing on the upper layer of the cell culture medium. As shown in Figure 4a and 4b, we performed MTT under normoxia and hypoxia, respectively. Under hypoxia, the IC_{50} of B, AB, DB and ADB to HepG2 are 3.15, 1.99, 1.99 and 1.25 μM. Meanwhile, the IC_{50} of B, AB, DB and ADB are 1.93, 1.90, 1.89 and 1.10 μM in normoxia. Under normoxia, no significant differences were detected in the cell viability of the B, AB and DB groups, while under hypoxia, AB, DB, and ADB all exhibit significantly enhanced phototoxicity than B, especially ADB can induce the strongest phototoxicity towards HepG2 cells.

We also evaluated the pathway to cell death using Annexin V-FITC/PI cell apoptosis detection kit. In Figure 4d, a total of 19 treatments were performed: PBS, ATO, 17-DMAG, N-D B, N-D AB, N-D DB, N-D ADB, H-D B, H-D AB, H-D DB, H-D ADB, N-L B, N-L AB, N-L DB, N-L ADB, H-L B, H-L AB, H-L DB, and H-L ADB. Among them, N-D represents normoxia without NIR, H-L represents hypoxia with NIR, and N-L represents normoxia with NIR. Regardless of hypoxia or normoxia, for each "L" group, many cells undergo apoptosis/necrosis. Among them, H-L ADB and N-L ADB have the highest proportion of apoptosis and necrosis, with only 12.4% and 6.08% of healthy cells. Amongst the other groups under hypoxia treatment, the apoptosis/necrosis rates of the H-L B, H-L AB, H-L DB and H-L ADB groups were 66.8%, 72.4%, 81.5% and 87.6%, respectively. The dual-drug loading nanococktail ADB can kill tumor cells, significantly better than the no-drug loading group and

14

any of the single-drug loading groups. Under hypoxia, it can be seen that the ATO-loaded group has an enhanced cell killing ability compared with the ATO-free group. Meanwhile, to analyze the influence from NIR irradiation, apoptosis analysis was conducted under hypoxia without NIR irradiation, resulting in 89.1%, 84.7%, 79.8%, and 75.9% of healthy cells in H-D B, H-D AB, H-D DB, and H-D ADB groups, respectively. Compared with the "H-L" groups, the proportion of healthy cells in the "H-D" groups is much higher.
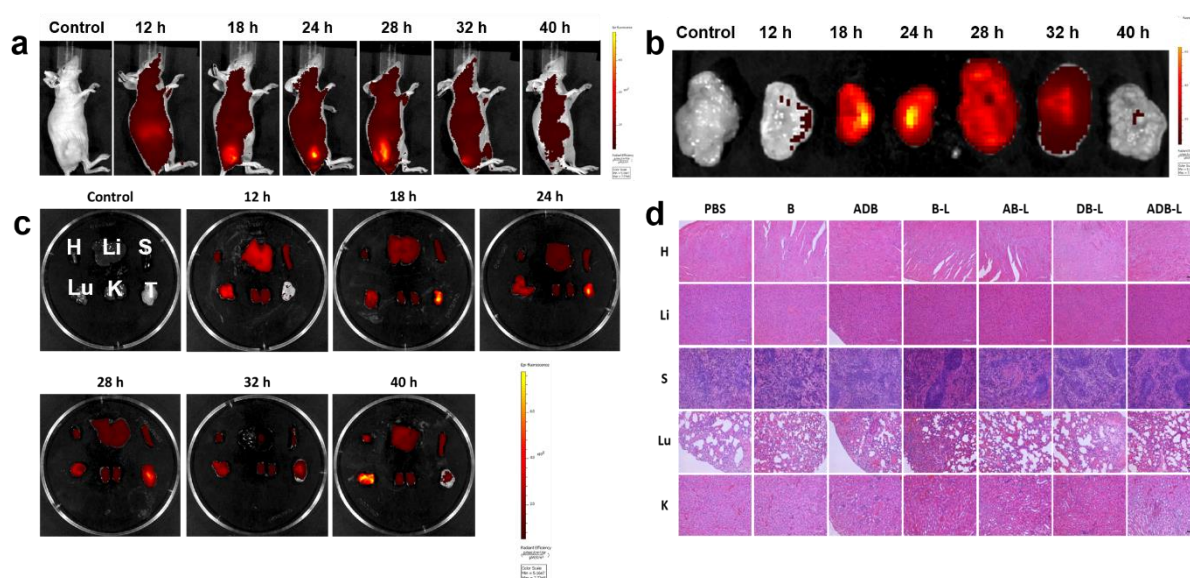
Figure 5. Tumor-targeting, biodistribution and biosafety *in vivo*. (a) Fluorescence imaging of HepG2 xenograft-bearing mice injected intravenously with ADB at various times: 12, 18, 24, 28, 32, and 40 h. (b) Fluorescence imaging of excised tumors after intravenous injection of ADB for various times. (c) Fluorescence imaging of organs and tumors after intravenous injection with ADB for various times. (d) Histological examination of the main organs from HepG2 xenograft-bearing mice treated with PBS, B, ADB, B-L, AB-L, DB-L, and ADB-L at 25 d post-injection. H: Heart, Li: Liver, S: Spleen, Lu: Lung, K: Kidney, T: Tumor. Scale bar, 100 μm.

Tumor accumulation, **biodistribution and biosafety.** To evaluate the tumor accumulation of ADB *in vivo*, ADB (equivalent concentration of BSL-1: 5 mg/kg·bw) was injected into mice

bearing HepG2 xenografts through the tail vein. At 12, 18, 24, 28, 32, and 40 h after injection, the small animal imaging system (IVIS Spectrum; Ex/Em: 675/695 nm) was used to observe the fluorescence signal of the tumor area. Obvious red fluorescence signal was captured at the tumor sites at 18, 24, and 28 h (Figure 5a). To determine the biodistribution of ADB, the tumors and various organs were collected for fluorescence imaging. Strong fluorescence was detected at the tumor sites 18 and 24 h after the tail vein injection (Figure 5b and Figure S17), meanwhile quite low fluorescence was detected in the organs (heart, liver, spleen, lung, and kidney) (Figure 5c), indicating that ADB can selectively accumulate in the tumor tissues. According to the above results, NIR irradiation was performed at 18 h or 24 h after injection in the subsequent experiments.

To evaluate the safety of each nanococktail based on BSL-1 *in vivo*, we analyzed the blood and blood biochemical indexes of the mice. Using hematology analysis, according to, all the parameters of blood data obtained in each group were within the normal range in Table S3. As well, there were no significant differences in clinical blood biochemical analysis (Table S4). Meanwhile, we stripped the heart, liver, spleen, lung, and kidney, and performed pathological biopsy by H&E staining to evaluate toxicity of various nanococktails *in vivo*. The results of the pathological biopsy indicated that the main organs of the mice in each group were stable in shape, and cellular structure of the main organic tissues was clear, which indicates that there was no significant tissue toxicity (Figure 5d). What's more, no significant difference in the body weight of the mice between the groups was detected (Figure S18). In summary, our nanococktails based on BSL-1 exhibit good biosafety, and do not cause significant toxicity *in vivo*.
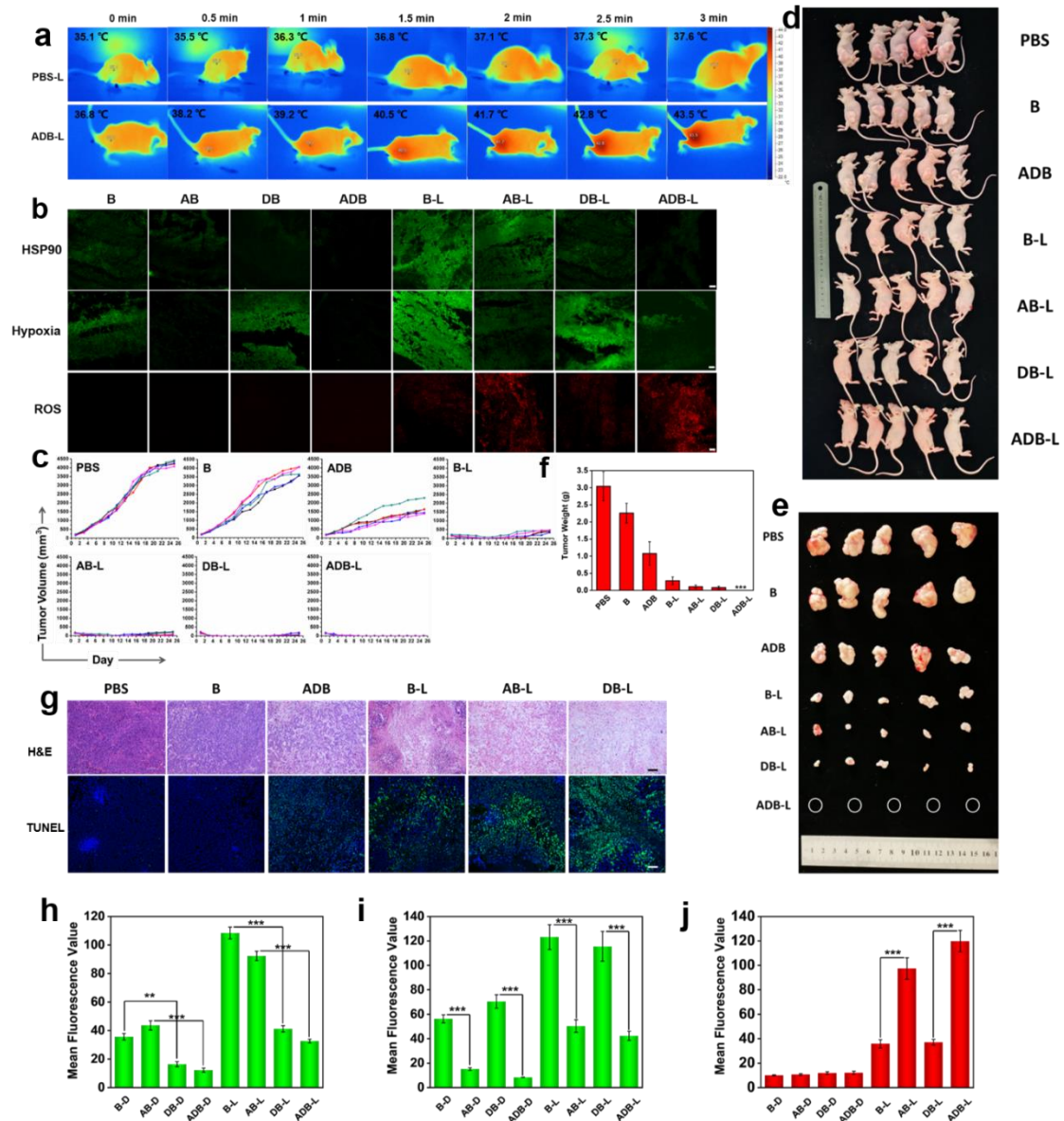
Figure 6. *In vivo* antitumor efficacy. (a) Infrared thermography at the tumor sites, NIR (685 nm, 1.5 W/cm^2, 3 min). (b) Expression of HSP90, hypoxia and ROS analysis of tumor sections by CLSM, NIR (685 nm, 1.5 W/cm^2, 3 min). Scale bar, 100 μm. (c) Tumor volume over 25 d of each mouse in B, AB, DB, ADB, B-L, AB-L, DB-L, and ADB-L groups. (d) Photographs of HepG2 xenografts-bearing mice in B, AB, DB, ADB, B-L, AB-L, DB-L, and ADB-L groups at 25 d post-injection. (e) Excised tumors in B, AB, DB, ADB, B-L, AB-L, DB-L, and ADB-L groups. (f) Excised tumor weight in B, AB, DB, ADB, B-L, AB-L, DB-L, and ADB-L groups (n = 5), ***$P < 0.001$. (g) H&E staining and TUNEL analysis of excised tumor sections in B, AB, DB, ADB, B-L, AB-L, and DB-L groups. Scale bar, 100 μm. (h) Mean fluorescence

17

intensity quantification of HSP90 in (b) (n = 3), **$P < 0.01$, ***$P < 0.001$. (i) Mean fluorescence intensity quantification of hypoxia in (b) (n = 3), ***$P < 0.001$. (j) Mean fluorescence intensity quantification of ROS in (b) (n = 3), ***$P < 0.001$.

***In vivo* antitumor efficacy.** In order to evaluate the photothermal efficacy of ADB *in vivo*, BALB/C nude mice bearing HepG2 xenografts were injected with ADB (equivalent concentration of BSL-1: 5 mg/kg·bw) into the tail vein. After 24 h, NIR irradiation (685 nm, 1.5 W/cm^2, 3 min) of the tumor site. Captured by an FLIR E4 infrared camera, the temperature of irradiated tumor site in the ADB group increased by 6 °C (from 36.8 °C to 42.8 °C) (ADB-L; Figure 6a). On the contrary, the PBS-L group exhibited a negligible change in temperature of 2.2 °C (from 35.1 °C to 37.3 °C) during the equivalent time of NIR irradiation (PBS-L; Figure 6a). The observed temperature increase of the irradiated tumor sites indicates that ADB exhibits a high level of photothermal conversion *in vivo*.

Since the generation of ROS correlates with the O$_2$ content of the tissue. Hypoxia probes can be used to assess the hypoxia status of the tumor sites of mice in B, AB, DB, and ADB groups with or without NIR irradiation. The ROS generation in each tumor tissue is used to determine whether the ATO-loaded nanococktails exhibit efficient PDT. The study found that tumor tissues of mice treated with ATO-containing nanococktails exhibited weaker green fluorescence at their tumor sites, indicating that ATO in the nanococktails can effectively relieve tissue hypoxia (Hypoxia; Figure 6b and 6i). The ROS generation at tumor sites of mice in B, AB, DB, and ADB groups with or without NIR irradiation was detected by dihydroethidium (DHE) staining (ROS; Figure 6b and 6j). In the NIR groups, red fluorescence was detected, indicating that nanococktails based on BSL-1 boost ROS generation under NIR irradiation, especially the AB-L and ADB-L groups, which exhibited strong red fluorescence, which was attributed to a remission in hypoxia and increase of ROS generation due to the ATO loaded in the nanococktails.

In addition, we also evaluated the expression of HSP90 to confirm whether 17-DMAG in the nanococktails can counteract the thermal resistance of the cells during PTT. The expression of HSP90 was analyzed by immunofluorescence. Strong green fluorescence was observed for the B-L and AB-L groups, and negligible fluorescence was observed for the B, AB, DB, ADB, DB-L and ADB-L groups. The HSP90 protein expression in the B-L and AB-L groups was up-regulated, while that in B, AB, DB, ADB, DB-L and ADB-L groups was down-regulated, which associated with the 17-DMAG loaded in the nanococktails inhibiting the expression of HSP90 (HSP90; Figure 6b and 6h).

Finally, the anti-tumor efficacy of the nanococktails with NIR irradiation was evaluated *in vivo*. 7 groups of mice were divided for tumor treatment: PBS, B, ADB, B-L, AB-L, DB-L and ADB-L. Compared with PBS and B groups, the tumor volume and weight of ADB, B-L, AB-L, DB-L and ADB-L groups (Figure 6c, 6d, 6e, and 6f) were significantly reduced. In addition, for the ADB-L group, the tumors of the mice disappeared completely (Figures 6c, 6d, 6e, and 6f). H&E staining and TUNEL staining further confirmed that the tumor sites of B-L, AB-L and DB-L groups exhibited obvious apoptosis compared with of the other groups (Figure 6g). In summary, nanococktails based on BSL-1 can effectively kill cancer cells *in vivo*, and in particular the dual-drug loaded ADB can completely eradicate tumors.

CONCLUSION

In summary, nanococktail ADB was fabricated by supramolecular glyco-assembly of BSL-1, ATO and 17-DMAG with hydrophilic lactose moiety and hydrophobic BODIPY block, which could facilitate uptake by hepatoma cells and enable controlled release into the cytoplasm. BSL-1 is composed of a hydrophilic lactose module for tumor targeting, disulfide bond to provide TME responsiveness, and hydrophobic BODIPY to provide synergistic PDT and PTT. The loaded ATO reduced the O_2 consumption of tumor cells, thereby alleviating hypoxia and enhancing the efficacy of PDT. Meanwhile, the 17-DMAG loading inhibited the expression of

HSP90 in tumor cells, thereby reducing thermal resistance to PTT, which can amplify the sensitivity of phototherapy, and reduce damage to normal tissue. Finally, the *in vivo* results indicated that ADB resulted in the complete ablation of tumor tissues under NIR irradiation and exhibited good anti-tumor efficiency and biosafety. Therefore, this research ameliorates the inherent shortcomings of phototherapy through the loading of two inhibitors with the supramolecular glyco-assembly, paving the way for the development of safe and effective phototherapeutic platforms for tumor eradication.

EXPERIMENTAL SECTION.

Synthesis of BSL-1. The synthesis of compound **9** follows a modified route based on the published method,[66] and the synthetic route is given in Figure S1. The detailed synthesis of compound **9** is described in supporting information. The ^{1}H NMR spectrum of compound **9** is given in Figure S2. The synthesis of compound BSL-1 follows a modified route based on the published method,[39] and the synthetic route is shown in Figure S1. The detailed synthesis of BSL-1 is described in supporting information. The ^{1}H NMR spectrum of BSL-1 is given in Figure S3. The ^{13}C NMR spectrum of BSL-1 is shown in Figure S4. The HRLC-MS spectrum of BSL-1 was shown in Figure S5. HRLC-MS (m/z): calcd for $[M+Na]^+$ $C_{60}H_{69}BN_6O_{19}F_2NaS_2^+$, 1313.4018; found 1313.4050.

Characterization of critical aggregation concentration of nanococktails based on BSL-1. BSL-1 aqueous solutions with different concentrations (2.5, 5, 7.5, 10, 20, 30, 40, 50 μM) were prepared for measurement of the surface tension, and then the abscissa as the concentration of the compound BSL-1 with the ordinate as the scatter plot of the surface tension was drawn. The appropriate points were selected to make two intersecting straight lines. The critical aggregation concentration from the intersection is 9.83 μM.

Dual-drug loading study. 0.367 mg ATO (1 μmol), 0.617 mg 17-DMAG (1 μmol) and 1.291

mg BSL-1 (1 μmol) were dissolved in 1 mL of water. The mixture was sonicated for 30 min and allowed to stand overnight to obtain the dual-drug-loaded nanosystem, which was purified by dialysis in distilled water (MW 8000) until the ATO and 17-DMAG in the water outside the dialysis bag displayed negligible UV/Vis changes. The amount of residual ATO and 17-DMAG in the dialysate is quantitatively measured by a microplate reader. The encapsulation efficiency and loading capacity of ATO and 17-DMAG can be calculated using the following formula:

Encapsulation efficiency (%) = loaded drug mass / input drug mass

Loading capacity (%) = loaded drug mass / mass of drug-loaded carriers

Morphology characterization of nanococktails. B, AB, DB, and ADB aqueous solution dispersion were dropped onto transmission electron microscope meshes (copper mesh, 300 mesh, surface carbon coating, microscope instrument). After sample preparation was completed, the transmission electron microscope was used to observe and take pictures. A ZEN3600 nano laser particle size analyzer was used to measure the particle size of the prepared nano-system aqueous solution, and the measurement was repeated three times.

Photodynamic property. DPBF is used to monitor the production of singlet oxygen ($^1O_2$). In short, 10 μM **1**, BSL-1 and methylene blue were mixed with 30 μM DPBF in water, and then irradiated for 60 s (685 nm, 0.08 W/cm^2). The absorbance of DPBF was monitored at 422 nm in 10 s intervals. The experiment was initially conducted in water with methylene blue (MB) as a reference (in water $\Phi_\Delta = 0.52$), using a 685 nm laser (0.08 W/cm^2) for irradiation. The $^1O_2$ quantum yields of BSL-1 and **1** was calculated to be 0.183 and 0.317, respectively.

Photothermal property. In order to evaluate the photothermal properties of our compound, a 685 nm laser (1.5 W/cm^2) was used to irradiate 8 mL PBS, BSL-1 (10 μM) and **1** (10 μM) in a glass vial for 30 min. At the same time, a thermometer was used to record the temperature of

all samples at 30 s intervals. According to the previous calculation method, we measured the light-to-heat conversion efficiency (η) of BSL-1 and **1**. The calculation of the η value is given according to previous method.[60] The photothermal conversion efficiencies of **1** and BSL-1 are 0.534 and 0.414, respectively.

Cellular uptake of B. According to previous report,[60] HepG2 cells were incubated with B for various times. After incubation, the cells were washed twice with cold PBS, and their uptake was analyzed by CLSM and FCM.

Study on the levels of hypoxia and ROS in cells. There were nine treatment groups: PBS, B-H, B-N, AB-H, AB-N, DB-H, DB-N, ADB-H, and ADB-N. To the B-H, B-N, AB-H, AB-N, DB-H, DB-N, ADB-H, and ADB-N groups B, B, AB, AB, DB, DB, ADB, and ADB in fresh medium were added (equivalent concentration of BSL-1: 2.5 μM) and cultured for 24 h, while the PBS group was added with the same amount of fresh PBS and cultured for 24 h. In the B-H, AB-H, DB-H and ADB-H groups, liquid paraffin was added to the culture medium to form an anoxic environment. NIR irradiation (685 nm, 0.08 W/cm^2) was performed for 20 min after replacement of fresh medium. Finally, CLSM was used to measure hypoxia and ROS in cells with the ROS-ID™ Hypoxia/Oxidative Stress Detection Kit. For the ROS probe, $\lambda_{ex} = 488$ nm. For the hypoxia probe, $\lambda_{ex} = 561$ nm.

Evaluation of HSP90 expression. There were four groups: B-L, AB-L, DB-L and ADB-L. RPMI-1640 medium containing B, AB, DB, and ADB (equivalent concentration of BSL-1: 2.5 μM) were used to incubate cells for 24 h. NIR irradiation (685 nm, 0.08 W/cm^2) was performed for 20 min after replacement of fresh medium. HSP90 expression were evaluated by immunofluorescence assay as previously reported.[60] Finally, HSP90 expression level of cells were detected by CLSM.

Evaluation of mitochondrial membrane potential. There were nine groups: PBS, B-H, B-N,

AB-H, AB-N, DB-H, DB-N, ADB-H, and ADB-N. To B-H, B-N, AB-H, AB-N, DB-H, DB-N, ADB-H, and ADB-N groups, fresh medium containing B, B, AB, AB, DB, DB, ADB, and ADB are added (equivalent concentration of BSL-1: 2.5 μM) cultured for 24 h, while the PBS group was added with the same amount of fresh PBS, and cultured for 24 h. In the B-H, AB-H, DB-H and ADB-H groups, liquid paraffin was added to the culture medium to form an anoxic environment. NIR irradiation (685 nm, 0.08 W/cm^2) was performed for 20 min after replacement of fresh medium. Finally, CLSM was used to measure mitochondrial membrane potential via JC-10 of the mitochondrial membrane potential detection kit. For JC-monomer, λ_{ex} = 488 nm. For JC-aggregates, λ_{ex} = 561 nm.

Evaluation of biocompatibility and cytotoxicity. The MTT method was used to evaluate the biocompatibility and cytotoxicity of ATO, 17-DMAG, B and various nanococktails (n = 6). Dark toxicity of B was evaluated using HepG2 and HL7702 cells cultured with medium containing 0, 0.25, 0.5, 0.75, 1, 1.25, 1.5, 2, 2.5, 5, 10, and 20 μM BSL-1. Evaluation of the toxicity of ATO, 17-DMAG, B, AB, and ADB to HL7702 and HepG2 cells were obtained with medium containing different concentrations of ATO, 17-DMAG, B, AB, DB, and ADB.

B, **AB**, **DB and ADB phototoxicity evaluation of HepG2 cells under hypoxia and normoxia.** The MTT method was used to evaluate phototoxicity of B, AB, DB, and ADB to HepG2 cells (n = 6). Phototoxicity of B, AB, DB, and ADB was evaluated using HepG2 cultured with medium containing various concentrations of B, AB, DB, and ADB. NIR irradiation (685 nm, 0.08 W/cm^2) was performed for 20 min under hypoxia and normoxia.

Evaluation of HepG2 cell apoptosis. For apoptosis detection of HepG2 cells, they were treated with Annexin V-FITC/PI apoptosis kit in 19 groups: PBS, ATO, 17-DMAG, N-D B, N-D AB, N-D DB, N-D ADB, H-D B, H-D AB, H-D DB, H-D ADB, N-L B, N-L AB, N-L DB, N-L ADB, H-L B, H-L AB, H-L DB, and H-L ADB. Among them, N-D represents the normoxia without

illumination group, H-L represents the hypoxia with illumination group, and N-L represents the normoxia with illumination group. NIR irradiation (685 nm, 0.08 W/cm^2) was performed for 20 min in "N-L" and "H-L" groups, and the "N-D" and "H-D" groups did not undergo irradiation treatment. Finally, the cells are analyzed by FCM according to Annexin V-FITC/PI apoptosis detection kit instructions.

***In vivo* tissue distributions.** BALB/C nude mice with HepG2 xenograft were injected intravenously with PBS or ADB (equivalent concentration of BSL-1: 5 mg/kg·bw) at predetermined time points (0, 12, 18, 24, 28, 32, and 40 h), then the fluorescence images of B were captured. The major organs and tumor tissues were extracted and fluorescence images captured. Then, the fluorescence intensity of B in mice and various tissues were measured using a PerkinElmer IVIS instrument.

***In vivo* hypoxia and ROS study.** The mice were treated differently and tested in 8 groups: B, B-L, AB, AB-L, DB, DB-L, ADB, and ADB-L. The hypoxia detection probe Hypoxyprobe^{TM}-1 was injected through the tail vein, and the ROS probe (DHE, 2 mg kg^{-1}) was injected into the tumor 24 h after intravenous injection of B, AB, DB, and ADB (equivalent concentration of BSL-1: 5 mg/kg·bw). NIR irradiation (685 nm, 1.5 W/cm^2) was performed for 3 min on the tumor sites. CLSM was used for hypoxia and ROS study on tumor tissues.

***In vivo* photothermal imaging.** For photothermographic imaging, BALB/C nude mice with HepG2 xenograft were injected intravenously with PBS or ADB (equivalent concentration of BSL-1: 5 mg/kg·bw). NIR irradiation (685 nm, 1.5 W/cm^2) was performed on tumor sites for 3 min 24 h after injection, and the photothermal imaging was recorded by FLIR E4 infrared camera every 30 s.

***In vivo* HSP90 expression.** The mice with HepG2 xenograft were treated differently and tested in 8 groups: B, B-L, AB, AB-L, DB, DB-L, ADB, and ADB-L. Mice were injected

intravenously with various nanococktails (equivalent concentration of BSL-1: 5 mg/kg·bw). NIR irradiation (685 nm, 1.5 W/cm^2) was performed on tumor sites for 3 min 24 h after injection in B-L, AB-L, DB-L, and ADB-L groups, and no irradiation was performed in B, AB, DB, ADB groups. Fluorescence immunoassays were performed for detection of HSP90 expression according to the previous report.[60] CLSM was used to detect the HSP90 expression levels in tumor tissues.

Biosafety evaluation of various nanococktails. The mice with HepG2 xenograft were randomly divided into 7 groups (n = 5 in each group): PBS, B, ADB, B-L, AB-L, DB-L, and ADB-L. The mice were intravenously injected with PBS or various nanococktails (equivalent concentration of BSL-1: 5 mg/kg·bw) when the tumor size reached 100-200 mm^3, the day was set as day 0. NIR irradiation (685 nm, 1.5 W/cm^2) was performed twice on tumor sites for 3 min at 18 h and 24 h after injection in B-L, AB-L, DB-L, and ADB-L groups, and no irradiation was performed in PBS, B, and ADB groups. After 6 days, the previous operation was repeated, except that irradiation of the "L" group was carried out only once at 24 h after the injection. Then a biochemical analyzer and a blood cell analyzer were used to analyze the blood until they were sacrificed on the 25th day. The major organs of each group were harvested for H&E.

In vivo **anti-tumor activity.** The mice with HepG2 xenograft were randomly divided into 7 groups (n = 5): PBS, B, ADB, B-L, AB-L, DB-L, and ADB-L. The treatment in each group was consistent with biosafety evaluation. The tumor volume and body weight were recorded every 2 days. The tumor size was measured by digital vernier calipers, and calculated using the following formula:

$$V = (L \times W^2)/2$$

Where L is the long diameter measured by a caliper, and W is the short diameter. The tumor tissues were collected, weighed and photographed.

The tumor tissues of each group were stained with H&E, and the pathological sections were observed by optical microscopy. Cell apoptosis in each group of solid tumor tissues were analyzed according to TUNEL staining. According to the instructions, we treated the paraffin-embedded tissue sections (20 μm) with TUNEL Apoptosis Detection Kit (Yeasen), and the sections were visualized under a fluorescence microscope.

ASSOCIATED CONTENT

Supporting Information. The Supporting Information is available free of charge at

https://pubs.acs.org/doi/xx.xxxx/acsami.xxxxx

AUTHOR INFORMATION

Corresponding Author

Yuxin Pei - Shaanxi Key Laboratory of Natural Products & Chemical Biology, College of Chemistry & Pharmacy, Northwest A&F University, Yangling, Shaanxi 712100, P. R. China; E-mail: peiyx@nwafu.edu.cn

Authors

Weiwei Feng - Shaanxi Key Laboratory of Natural Products & Chemical Biology, College of Chemistry & Pharmacy, Northwest A&F University, Yangling, Shaanxi 712100, P. R. China

Shangqian Zhang - Shaanxi Key Laboratory of Natural Products & Chemical Biology, College of Chemistry & Pharmacy, Northwest A&F University, Yangling, Shaanxi 712100, P. R. China

Yichen Wan - Shaanxi Key Laboratory of Natural Products & Chemical Biology, College of Chemistry & Pharmacy, Northwest A&F University, Yangling, Shaanxi 712100, P. R. China

Zelong Chen - Shaanxi Key Laboratory of Natural Products & Chemical Biology, College of Chemistry & Pharmacy, Northwest A&F University, Yangling, Shaanxi 712100, P. R. China

Yun Qu - Shaanxi Key Laboratory of Natural Products & Chemical Biology, College of Chemistry & Pharmacy, Northwest A&F University, Yangling, Shaanxi 712100, P. R. China

Jiahui Li - Shaanxi Key Laboratory of Natural Products & Chemical Biology, College of Chemistry & Pharmacy, Northwest A&F University, Yangling, Shaanxi 712100, P. R. China

Tony D. James - Department of Chemistry, University of Bath, Bath, BA7 7AY, UK

Zhichao Pei - Shaanxi Key Laboratory of Natural Products & Chemical Biology, College of Chemistry & Pharmacy, Northwest A&F University, Yangling, Shaanxi 712100, P. R. China

Author Contributions

[#]W. F. and S. Z. contributed equally to this work.

Notes

The authors declare no competing financial interest

REFERENCES

1.   Chen, S.; Zhong, Y.; Fan, W.; Xiang, J.; Wang, G.; Zhou, Q.; Wang, J.; Geng, Y.; Sun, R.; Zhang, Z.; Piao, Y.; Wang, J.; Zhuo, J.; Cong, H.; Jiang, H.; Ling, J.; Li, Z.; Yang, D.; Yao, X.; Xu, X.; Zhou, Z.; Tang, J.; Shen, Y. Enhanced Tumour Penetration and Prolonged Circulation in Blood of Polyzwitterion-Drug Conjugates with Cell-Membrane Affinity *Nat. Biomed. Eng.* **2021**, *5*, 1019-1037.

2.   Chen, J.; Qiu, M.; Ye, Z.; Nyalile, T.; Li, Y.; Glass, Z.; Zhao, X.; Yang, L.; Chen, J.; Xu, Q. In situ Cancer Vaccination Using Lipidoid Nanoparticles *Sci. Adv.* **2021**, *7*, eabf1244.

3.   Wu, X.; Tan, Y. J.; Toh, H. T.; Nguyen, L. H.; Kho, S. H.; Chew, S. Y.; Yoon, H. S.; Liu, X. W. Stimuli-Responsive Multifunctional Glyconanoparticle Platforms for Targeted Drug Delivery and Cancer Cell Imaging *Chem. Sci.* **2017**, *8*, 3980-3988.

4.   Hu, X.-Y.; Gao, L.; Mosel, S.; Ehlers, M.; Zellermann, E.; Jiang, H.; Knauer, S. K.; Wang, L.; Schmuck, C. From Supramolecular Vesicles to Micelles: Controllable Construction of Tumor-Targeting Nanocarriers based on Host-Guest Interaction between a Pillar[5]arene-based Prodrug and a RGD-Sulfonate Guest *Small* **2018**, *14*, e1803952.

5.   Zhou, J.; Rao, L.; Yu, G.; Cook, T. R.; Chen, X.; Huang, F. Supramolecular Cancer Nanotheranostics *Chem. Soc. Rev.* **2021**, *50*, 2839-2891.

6.   Hao, L.; Zhou, Q.; Piao, Y.; Zhou, Z.; Tang, J.; Shen, Y. Albumin-binding Prodrugs via Reversible Iminoboronate forming Nanoparticles for Cancer Drug Delivery *J. Control Release* **2021**, *330*, 362-371.

7.   Shao, Y.; Guo, L.; Li, A.; Zhang, K.; Liu, W.; Shi, J.; Liu, J.; Zhang, Z. US-Triggered Ultra-Sensitive "Thrombus Constructor" for Precise Tumor Therapy *J. Control Release* **2020**, *318*, 136-144.

8.   Hao, Q.; Wang, Z.; Zhao, W.; Wen, L.; Wang, W.; Lu, S.; Xing, D.; Zhan, M.; Hu, X. Dual-Responsive Polyprodrug Nanoparticles with Cascade-Enhanced Magnetic Resonance Signals for Deep-Penetration Drug Release in Tumor Therapy *ACS Appl. Mater. Interfaces* **2020**, *12*, 49489-49501.

9.   Miranda, D.; Carter, K.; Luo, D.; Shao, S.; Geng, J.; Li, C.; Chitgupi, U.; Turowski, S. G.; Li, N.; Atilla-Gokcumen, G. E.; Spernyak, J. A.; Lovell, J. F. Multifunctional Liposomes for Image-Guided Intratumoral Chemo-Phototherapy *Adv. Healthc. Mater.* **2017**, *6*, 201700253.

10.   Amaral, S. I.; Costa-Almeida, R.; Gonçalves, I. C.; Magalhães, F. D.; Pinto, A. M., Carbon Nanomaterials for Phototherapy of Cancer and Microbial Infections *Carbon* **2022**, *190*, 194-244.

11. Mauro, N.; Utzeri, M. A.; Sciortino, A.; Messina, F.; Cannas, M.; Popescu, R.; Gerthsen, D.; Buscarino, G.; Cavallaro, G.; Giammona, G. Decagram-Scale Synthesis of Multicolor Carbon Nanodots: Self-Tracking Nanoheaters with Inherent and Selective Anticancer Properties *ACS Appl. Mater. Interfaces* **2022**, *14*, 2551-2563.

12. Einafshar, E.; Asl, A. H.; Nia, A. H.; Mohammadi, M.; Malekzadeh, A.; Ramezani, M. New Cyclodextrin-based Nanocarriers for Drug Delivery and Phototherapy using an Irinotecan Metabolite *Carbohyd. Polym.* **2018**, *194*, 103-110.

13. Song, N.; Zhang, Z.; Liu, P.; Dai, D.; Chen, C.; Li, Y.; Wang, L.; Han, T.; Yang, Y. W.; Wang, D.; Tang, B. Z. Pillar[5]arene-Modified Gold Nanorods as Nanocarriers for Multi‐Modal Imaging-Guided Synergistic Photodynamic-Photothermal Therapy *Adv. Funct. Mater.* **2021**, *31*, 2009924.

14. Cheng, Q.; Yue, L.; Li, J.; Gao, C.; Ding, Y.; Sun, C.; Xu, M.; Yuan, Z.; Wang, R. Supramolecular Tropism Driven Aggregation of Nanoparticles in situ for Tumor-Specific Bioimaging and Photothermal Therapy *Small* **2021**, e2101332.

15. Xie, Z.; Fan, T.; An, J.; Choi, W.; Duo, Y.; Ge, Y.; Zhang, B.; Nie, G.; Xie, N.; Zheng, T.; Chen, Y.; Zhang, H.; Kim, J. S. Emerging Combination Strategies with Phototherapy in Cancer Nanomedicine *Chem. Soc. Rev.* **2020**, *49*, 8065-8087.

16. Li, X.; Lee, S.; Yoon, J. Supramolecular Photosensitizers Rejuvenate Photodynamic Therapy *Chem. Soc. Rev.* **2018**, *47*, 1174-1188.

17. Kim, M.; Lee, J. H.; Nam, J. M. Plasmonic Photothermal Nanoparticles for Biomedical Applications *Adv. Sci.* **2019**, *6*, 1900471.

18. Zhen, X.; Xie, C.; Pu, K. Temperature-Correlated Afterglow of a Semiconducting Polymer Nanococktail for Imaging-Guided Photothermal Therapy *Angew. Chem. Int. Ed. Engl.* **2018**, *57*, 3938-3942.

19.   Li, J.; Cui, D.; Jiang, Y.; Huang, J.; Cheng, P.; Pu, K. Near-Infrared Photoactivatable Semiconducting Polymer Nanoblockaders for Metastasis-Inhibited Combination Cancer Therapy *Adv. Mater.* **2019**, *31*, e1905091.

20.   Yao, C.; Li, Y.; Wang, Z.; Song, C.; Hu, X.; Liu, S. Cytosolic NQO1 Enzyme-Activated Near-Infrared Fluorescence Imaging and Photodynamic Therapy with Polymeric Vesicles *ACS Nano* **2020**, *14*, 1919-1935.

21.   Zhang, Y.; He, X.; Zhang, Y.; Zhao, Y.; Lu, S.; Peng, Y.; Lu, L.; Hu, X.; Zhan, M. Native Mitochondria-Targeting Polymeric Nanoparticles for Mild Photothermal Therapy Rationally Potentiated with Immune Checkpoints Blockade to Inhibit Tumor Recurrence and Metastasis *Chem. Eng. J.* **2021**, *424*, 130171.

22.   Wang, Z.; Zhan, M.; Li, W.; Chu, C.; Xing, D.; Lu, S.; Hu, X. Photoacoustic Cavitation-Ignited Reactive Oxygen Species to Amplify Peroxynitrite Burst by Photosensitization-Free Polymeric Nanocapsules *Angew. Chem. Int. Ed. Engl.* **2021**, *60*, 4720-4731.

23.   Xu, C.; Jiang, Y.; Huang, J.; Huang, J.; Pu, K. Second Near-Infrared Light-Activatable Polymeric Nanoantagonist for Photothermal Immunometabolic Cancer Therapy *Adv. Mater.* **2021**, *33*, e2101410.

24.   Xu, C.; Pu, K. Second Near-Infrared Photothermal Materials for Combinational Nanotheranostics *Chem. Soc. Rev.* **2021**, *50*, 1111-1137.

25.   Xu, M.; Zhang, C.; Zeng, Z.; Pu, K. Semiconducting Polymer Nanoparticles as Activatable Nanomedicines for Combinational Phototherapy *ACS Appl. Polym. Mater.* **2021**, *3*, 4375-4389.

26.   Nurunnabi, M.; Khatun, Z.; Reeck, G. R.; Lee, D. Y.; Lee, Y.-k. Photoluminescent Graphene Nanoparticles for Cancer Phototherapy and Imaging *ACS Appl. Mater. Interfaces* **2014**, *6*, 12413-12421.

27.   Taratula, O.; Doddapaneni, B. S.; Schumann, C.; Li, X.; Bracha, S.; Milovancev, M.; Alani, A. W. G.; Taratula, O. Naphthalocyanine-based Biodegradable Polymeric Nanoparticles for Image-Guided Combinatorial Phototherapy *Chem. Mater.* **2015**, *27*, 6155-6165.

28.   Chakrabortty, S.; Agrawalla, B. K.; Stumper, A.; Vegi, N. M.; Fischer, S.; Reichardt, C.; Kögler, M.; Dietzek, B.; Feuring-Buske, M.; Buske, C.; Rau, S.; Weil, T. Mitochondria Targeted Protein-Ruthenium Photosensitizer for Efficient Photodynamic Applications *J. Am. Chem. Soc.* **2017**, *139*, 2512-2519.

29.   Ivanova, V. A.; Verenikina, E. V.; Nikitina, V. P.; Zhenilo, O. E.; Kruze, P. A.; Nikitin, I. S.; Kit, O. I. Photodynamic Therapy for Preinvasive Cervical Cancer *J.Clin. Oncol.* **2020**, *38*, 6035-6035.

30.   Kessel, D.; Reiners, J. J. Photodynamic Therapy: Autophagy and Mitophagy, Apoptosis and Paraptosis *Autophagy* **2020**, *16*, 2098-2101.

31.   Lim, R. K.; Weinstock, M. A. Photodynamic Therapy and Medicare Expenditures *JAMA Dermatol.* **2021**, *157*, 356-357.

32.   Mishchenko, T. A.; Balalaeva, I. V.; Vedunova, M. V.; Krysko, D. V. Ferroptosis and Photodynamic Therapy Synergism: Enhancing Anticancer Treatment *Trend Cancer* **2021**, *7*, 484-487.

33.   Overchuk, M.; Cheng, M. H. Y.; Zheng, G. X-Ray-Activatable Photodynamic Nanoconstructs *ACS Cent. Sci.* **2020**, *6*, 613-615.

34.   Liu, Y.; Li, X.; Shi, Y.; Wang, Y.; Zhao, X.; Gong, X.; Cai, R.; Song, G.; Chen, M.; Zhang, X. Two-Dimensional Intermetallic Ptbi/Pt Core/Shell Nanoplates Overcome Tumor Hypoxia for Enhanced Cancer Therapy *Nanoscale* **2021**, *13*, 14245-14253.

35.   Zhang, M.; Wang, W.; Wu, F.; Zheng, T.; Ashley, J.; Mohammadniaei, M.; Zhang, Q.; Wang, M.; Li, L.; Shen, J.; Sun, Y. Biodegradable Poly(Gamma-Glutamic Acid)@Glucose Oxidase@Carbon Dot Nanoparticles for Simultaneous Multimodal Imaging and Synergetic Cancer Therapy *Biomaterials* **2020**, *252*, 120106.

36.   Li, M.; Li, S.; Zhou, H.; Tang, X.; Wu, Y.; Jiang, W.; Tian, Z.; Zhou, X.; Yang, X.; Wang, Y. Chemotaxis-Driven Delivery of Nano-Pathogenoids for Complete Eradication of Tumors Post-Phototherapy *Nat. Commun.* **2020**, *11*, 1126.

37.   Wang, Z.; Ju, Y.; Ali, Z.; Yin, H.; Sheng, F.; Lin, J.; Wang, B.; Hou, Y. Near-Infrared Light and Tumor Microenvironment Dual Responsive Size-Switchable Nanocapsules for Multimodal Tumor Theranostics *Nat. Commun.* **2019**, *10* , 4418.

38.   Zhang, W.; Hu, X.; Shen, Q.; Xing, D. Mitochondria-Specific Drug Release and Reactive Oxygen Species Burst Induced by Polyprodrug Nanoreactors Can Enhance Chemotherapy *Nat. Commun.* **2019**, *10*, 1704.

39.   Cheng, Y.; Kong, X.; Chang, Y.; Feng, Y.; Zheng, R.; Wu, X.; Xu, K.; Gao, X.; Zhang, H. Spatiotemporally Synchronous Oxygen Self-Supply and Reactive Oxygen Species Production on Z-Scheme Heterostructures for Hypoxic Tumor Therapy *Adv. Mater.* **2020**, *32*, e1908109.

40.   Wang, J.; Sun, J.; Hu, W.; Wang, Y.; Chou, T.; Zhang, B.; Zhang, Q.; Ren, L.; Wang, H. A Porous Au@Rh Bimetallic Core-Shell Nanostructure as an H_2O_2-Driven Oxygenerator to Alleviate Tumor Hypoxia for Simultaneous Bimodal Imaging and Enhanced Photodynamic Therapy *Adv. Mater.* **2020**, *32*, e2001862.

41.   Liu, Y.; Jiang, Y.; Zhang, M.; Tang, Z.; He, M.; Bu, W. Modulating Hypoxia via Nanomaterials Chemistry for Efficient Treatment of Solid Tumors *Acc. Chem. Res.* **2018**, *51*, 2502-2511.

42.   Sun, Q.; Wang, Z.; Liu, B.; Jia, T.; Wang, C.; Yang, D.; He, F.; Gai, S.; Yang, P. Self-Generation of Oxygen and Simultaneously Enhancing Photodynamic Therapy and MRI Effect: an Intelligent Nanoplatform to Conquer Tumor Hypoxia for Enhanced Phototherapy *Chem. Eng. J.* **2020**, *390*, 124624. .

43.   Gao, G.; Jiang, Y. W.; Sun, W.; Guo, Y.; Jia, H. R.; Yu, X. W.; Pan, G. Y.; Wu, F. G. Molecular Targeting-Mediated Mild-Temperature Photothermal Therapy with a Smart Albumin-based Nanodrug *Small* **2019**, *15*, e1900501.

44.   Li, B.; Hao, G.; Sun, B.; Gu, Z.; Xu, Z. P. Engineering a Therapy-Induced "Immunogenic Cancer Cell Death" Amplifier to Boost Systemic Tumor Elimination *Adv. Funct. Mater.* **2020**, *30*, 1909745.

45.   Liu, C.; Cao, Y.; Cheng, Y.; Wang, D.; Xu, T.; Su, L.; Zhang, X.; Dong, H. An Open Source and Reduce Expenditure ROS Generation Strategy for Chemodynamic/Photodynamic Synergistic Therapy *Nat. Commun.* **2020**, *11*, 1735.

46.   Feng, J.; Yu, W.; Xu, Z.; Wang, F. An Intelligent ZIF-8-Gated Polydopamine Nanoplatform for *in vivo* Cooperatively Enhanced Combination Phototherapy *Chem. Sci.* **2020**, *11*, 1649-1656.

47.   Liu, C. P.; Wu, T. H.; Liu, C. Y.; Chen, K. C.; Chen, Y. X.; Chen, G. S.; Lin, S. Y. Self-Supplying O_2 through the Catalase-Like Activity of Gold Nanoclusters for Photodynamic Therapy against Hypoxic Cancer Cells *Small* **2017**, *13*, 1700278.

48.   Zhou, J.; Liu, Y.; Zhang, G.; Jia, Q.; Li, L. DNA-Templated Porous Nanoplatform towards Programmed "Double-Hit" Cancer Therapy via Hyperthermia and Immunogenicity Activation *Biomaterials* **2019**, *219*, 119395.

49.   Zhao, H.; Li, L.; Zhang, J.; Zheng, C.; Ding, K.; Xiao, H.; Wang, L.; Zhang, Z. C-C Chemokine Ligand 2 (CCL2) Recruits Macrophage-Membrane-Camouflaged Hollow Bismuth Selenide Nanoparticles to Facilitate Photothermal Sensitivity and Inhibit Lung Metastasis of Breast Cancer *ACS Appl. Mater. Interfaces* **2018**, *10*, 31124-31135.

50.   Li, X.; Kwon, N.; Guo, T.; Liu, Z.; Yoon, J. Innovative Strategies for Hypoxic-Tumor Photodynamic Therapy *Angew. Chem. Int. Ed. Engl.* **2018**, *57*, 11522-11531.

51.   Zou, J.; Zhu, J.; Yang, Z.; Li, L.; Fan, W.; He, L.; Tang, W.; Deng, L.; Mu, J.; Ma, Y.; Cheng, Y.; Huang, W.; Dong, X.; Chen, X. A Phototheranostic Strategy to Continuously

Deliver Singlet Oxygen in the Dark and Hypoxic Tumor Microenvironment *Angew. Chem. Int. Ed. Engl.* **2020**, *59*, 8833-8838.

52.   Wang, D.; Wu, H.; Phua, S. Z. F.; Yang, G.; Qi Lim, W.; Gu, L.; Qian, C.; Wang, H.; Guo, Z.; Chen, H.; Zhao, Y. Self-Assembled Single-Atom Nanozyme for Enhanced Photodynamic Therapy Treatment of Tumor *Nat. Commun.* **2020**, *11*, 357.

53.   Xia, D.; Xu, P.; Luo, X.; Zhu, J.; Gu, H.; Huo, D.; Hu, Y. Overcoming Hypoxia by Multistage Nanoparticle Deliviery System to Inhibit Mitochondrial Respiration for Photodynamic Therapy *Adv. Funct. Mater.* **2019**, *29*, 1807294.

54.   Fan, Y. T.; Zhou, T. J.; Cui, P. F.; He, Y. J.; Chang, X.; Xing, L.; Jiang, H. L. Modulation of Intracellular Oxygen Pressure by Dual-Drug Nanoparticles to Enhance Photodynamic Therapy *Adv. Funct. Mater.* **2019**, *29*, 1806708.

55.   Yang, G. G.; Zhou, D. J.; Pan, Z. Y.; Yang, J.; Zhang, D. Y.; Cao, Q.; Ji, L. N.; Mao, Z. W. Multifunctional Low-Temperature Photothermal Nanodrug with *in vivo* Clearance, ROS-Scavenging and Anti-Inflammatory Abilities *Biomaterials* **2019**, *216*, 119280.

56.   Dang, J.; Ye, H.; Li, Y.; Liang, Q.; Li, X.; Yin, L. Multivalency-Assisted Membrane-Penetrating Sirna Delivery Sensitizes Photothermal Ablation via Inhibition of Tumor Glycolysis Metabolism *Biomaterials* **2019**, *223*, 119463.

57.   Zhu, H.; Wang, H.; Shi, B.; Shangguan, L.; Tong, W.; Yu, G.; Mao, Z.; Huang, F. Supramolecular Peptide Constructed by Molecular Lego Allowing Programmable Self-Assembly for Photodynamic Therapy *Nat. Commun.* **2019**, *10*, 2412.

58.   Shi, C.; Li, M.; Zhang, Z.; Yao, Q.; Shao, K.; Xu, F.; Xu, N.; Li, H.; Fan, J.; Sun, W.; Du, J.; Long, S.; Wang, J.; Peng, X. Catalase-based Liposomal for Reversing Immunosuppressive Tumor Microenvironment and Enhanced Cancer Chemo-Photodynamic Therapy *Biomaterials* **2020**, *233*, 119755.

59.   He, Z.; Zhao, L.; Zhang, Q.; Chang, M.; Li, C.; Zhang, H.; Lu, Y.; Chen, Y. An Acceptor-Donor-Acceptor Structured Small Molecule for Effective NIR Triggered Dual Phototherapy of Cancer *Adv. Funct. Mater.* **2020**, *30*, 1910301.

60.   Feng, W.; Lv, Y.; Chen, Z.; Wang, F.; Wang, Y.; Pei, Y.; Jin, W.; Shi, C.; Wang, Y.; Qu, Y.; Ji, W.; Pu, L.; Liu, X.-W.; Pei, Z. A Carrier-Free Multifunctional Nano Photosensitizer based on Self-Assembly of Lactose-Conjugated BODIPY for Enhanced Anti-Tumor Efficacy of Dual Phototherapy *Chem. Eng. J.* **2021**, *417*, 129178.

61.   Zhou, X.; Liu, Y.; Wang, X.; Li, X.; Xiao, B. Effect of Particle Size on the Cellular Uptake and Anti-Inflammatory Activity of Oral Nanotherapeutics. *Colloids Surf. B Biointerfaces* **2020**, *187*, 110880.

62.   Meena, J.; Goswami, D. G.; Anish, C.; Panda, A. K. Cellular Uptake of Polylactide Particles Induces Size Dependent Cytoskeletal Remodeling in Antigen Presenting Cells. *Biomater. Sci.* **2021**, *9*, 7962-7976.

63.   Mosquera, J.; García, I.; Liz-Marzán, L. M. Cellular Uptake of Nanoparticles versus Small Molecules: A Matter of Size. *Acc. Chem. Res.* **2018**, *51*, 2305-2313.

64.   Ruan, Z.; Yuan, P.; Li, T.; Tian, Y.; Cheng, Q.; Yan, L. Redox-Responsive Prodrug-Like Pegylated Macrophotosensitizer Nanoparticles for Enhanced Near-Infrared Imaging-Guided Photodynamic Therapy *Eur. J. Pharm. Biopharm.* **2019**, *135*, 25-35.

65.   Liu, Y.; Ai, K.; Liu, J.; Deng, M.; He, Y.; Lu, L. Dopamine-Melanin Colloidal Nanospheres: an Efficient Near-Infrared Photothermal Therapeutic Agent for *in vivo* Cancer Therapy *Adv. Mater.* **2013**, *25*, 1353-1359.

66.   Cao, S.; Pei, Z.; Xu, Y.; Pei, Y. Glyco-Nanovesicles with Activatable Near-Infrared Probes for Real-Time Monitoring of Drug Release and Targeted Delivery *Chem. Mater.* **2016**, *28*, 4501-4506.

Table Of Contents